Computer Modeling in Engineering & Sciences

Tech Science Press

https://doi.org/10.32604/cmes.2026.080540

ARTICLE

Enhancement of the Total Least Squares Method for Feature Extraction in 2D LiDAR Mapped Environments

Natalia Prieto-Fernández[1], Martín Bayón-Gutiérrez[1,*], Sergio Fernández-Blanco[1], Álvaro Fernández-Blanco[1], Francisco Carro-De-Lorenzo[2] and José Alberto Benítez-Andrades[1]

[1]Department of Electrical, Systems and Automatics Engineering, Universidad de León, León, Spain
[2]TRESCA Ingeniería S.A., León, Spain

*Corresponding Author: Martín Bayón-Gutiérrez. Email: martin.bayon@unileon.es

Received: 11 February 2026; Accepted: 15 April 2026; Published: 27 May 2026

ABSTRACT: Feature-based Simultaneous Localization and Mapping (SLAM) using 2D Light Detection and Ranging (LiDAR) in structured indoor environments commonly relies on the extraction of straight segments and corners from raw scan data. The quality of these landmarks depends not only on the fitting algorithm, but also on how uncertainty is modeled and propagated from line estimates to derived corner features. Although the magnitude of LiDAR uncertainty has been widely studied, the influence of line parameterization and geometric conditioning on uncertainty propagation has received less attention. In particular, the scale ambiguity inherent to implicit line representations can degrade numerical conditioning and affect the stability of the propagated covariance estimates. This paper proposes a novel Weighted Conformal Total Least Squares (WCTLS) formulation for line extraction from 2D LiDAR data. Unlike conventional approaches, the proposed method enforces a geometrical normalization that removes scale ambiguity and improves the conditioning of the estimation problem. The method is compared with Unweighted Total Least Squares (UTLS) and Weighted Total Least Squares (WTLS) using real indoor datasets and repeated scans acquired from fixed sensor positions. The results show that all three formulations provide equivalent geometric corner locations, whereas the proposed WCTLS method consistently reduces the propagated uncertainty of the estimated corner coordinates. In addition, repeatability analysis over 100 scans per environment shows that WCTLS yields lower median corner ellipse areas and reduced dispersion across scans, without increasing computational complexity.

KEYWORDS: Feature extraction; geometric primitives; light detection and ranging (LiDAR) mapping; total least squares (TLS)

1 Introduction

Simultaneous Localization and Mapping (SLAM) techniques have become a fundamental research area in autonomous robotics. They enable robots and vehicles to move autonomously in unknown environments, while also building a detailed map of their surroundings in real time. Its field of application spans beyond robotics. It is common to employ SLAM techniques in areas ranging from autonomous driving [1–3] and augmented reality systems [4] to remote hostile environment exploration [5]. For these purposes, the system must be equipped with appropriate sensors. The most common choices are GNSS (Global Navigation Satellite System), inertial navigation systems, cameras, RADAR (Radio Detection and Ranging), and LiDAR (Light Detection and Ranging). Sensors are selected according to the environmental characteristics to be mapped. In GNSS-denied environments where the satellite signal is lost, LiDAR sensors are a suitable alternative. They generate a two-dimensional representation of the environment from which to accurately estimate the

position and orientation of the robotic element in real time. Inertial sensors, which accumulate drift, and cameras, conditioned by visibility, are typically less efficient options [6].

The ability of these sensors to provide accurate and detailed data in real time has led to their use in numerous robotic platforms [6–8]. The rangefinder that equips the LiDAR sensor emits infrared laser signals that are reflected by the surroundings. Its receiver picks up these reflected waves, and its processor estimates the distance of the target from the sensor [3] by measuring the time-of-flight (TOF) of the signal. Additionally, an encoder provides angle measurement for each observed target. The sensor delivers a raw modulus-phase polar representation of the environment profile, which is processed into a map. LiDAR sensors capture information at high resolution. This contributes significantly to the quality of the generated maps, which is essential in applications that demand a detailed representation of the explored spaces. Recent research, such as [9], Zou et al. [10], and Kim et al. [11], has addressed issues related to the effective integration of LiDAR sensors into SLAM algorithms in order to improve the robustness and accuracy of positioning.

Despite its advantages, processing and storing large volumes of LiDAR data present challenges, especially in terms of computational resources. There are two main approaches regarding the transformation of raw data into usable maps: scan matching or feature extraction [12]. The first option revolves around the comparison of point clouds to complete the profile of the environment, with ICP (Iterative Closest Point) the most commonly used algorithm. These methods are typically overwhelmed by the computational strain as point clouds become larger [13]. In contrast, feature extraction methods extract the geometric features defining the environment, thus reducing the volume of data to be processed during subsequent stages. Such approaches significantly mitigate processing burdens within structured environments, where feature variability is reduced to straight segments, and their intersections [14].

Feature extraction techniques eventually yield a limited number of representative points on the map, which then serve as references for positioning. These points are necessarily obtained with associated estimation uncertainty, which is typically represented through covariance matrices. These covariance matrices are subsequently propagated during the estimation of successive robot poses along a trajectory and to new references generated in successive remapping steps. The estimation of covariance matrices associated with geometric features derived from LiDAR measurement standard deviations has been addressed by several authors [15–18], and their propagation to segment intersections has been addressed in [17–19]. Methodologies employed significantly condition the final results.

In this article, we propose a framework for estimating lines and corners as well as their uncertainties, which we have called Weighted Conformal Total Least Squares (WCTLS), inspired by the formulation in [20], but extended to explicitly incorporate measurement weighting and geometric normalization. The proposed approach removes scale ambiguity and improves the conditioning of the estimation problem. A comparative evaluation against the classic formulations of Unweighted Total Least Squares (UTLS) and Weighted Total Least Squares (WTLS) demonstrates that WCTLS yields lower corner uncertainty. These results show that the choice of geometric parameterization impacts the propagation of uncertainty and the reliability of landmarks in LiDAR-based SLAM.

2 Related Work

Feature extraction methods perform two separate steps. In a first iteration, raw data is segmented into separate geometric features. Afterwards, the parameters that define each of them are characterized.

2.1 Feature Detection Algorithms

A geometric feature, also known as a geometric primitive, is a set of measured neighbouring points with common properties, such as orientation or density, that identify regions such as walls or flat surfaces. The most common criterion to define these sets is their belonging to the same straight section. This refinement process performed on raw data is known as segmentation [14]. Nguyen et al. [21] collect the classical straight section extraction algorithms: Split-and-Merge [22] based on the detection of new line segments in those points whose distance to the straight line constituted by all of them exceeds a certain threshold, Hough Transform [23], Line-Regression [15], Random Sample Consensus (RANSAC) [24] and Expectation-Maximitation (EM) [25].

Other algorithms for line extraction have been described by Siadat et al. [20]. Iterative End Point Fit (IEPF) [26], a variant of Split-and-Merge where the line is constructed from the first and the last point. Successive Edge Following (SEF) [20] focuses on determining whether the difference between the distance from one point and the distance to the next exceeds a certain threshold. Line Tracking (LT) [20] uses the distance from the point to the segment constituted by the previous points as a segmentation parameter.

These algorithms have been widely used in the mapping process from 2D LiDAR data. The works of Nguyen et al. [21], Borges and Aldon [27], Peter et al. [28], or Prieto-Fernández et al. [17] are examples of research conducted using them as a basis.

Recent advances in LiDAR perception have also explored semantic segmentation of point clouds to identify structural elements of the environment. For example, Li et al. [29] use semantic segmentation to isolate building surfaces for map-based localization, while Deng et al. [30] propose a semantic enhancement network to improve object recognition in LiDAR data under challenging conditions. Although these approaches focus on high-level semantic understanding, they further highlight the importance of reliable feature detection and segmentation in LiDAR-based perception systems.

2.2 Feature Parameterization Algorithms

Once the environment has been segmented, the geometric features that define each segment are extracted along with their associated covariance matrices. This way, a large volume of data is condensed into a reduced number of parameters. The computational burden in subsequent processes is thus significantly reduced [31].

One of the most common methods for feature extraction is line detection, which is considered to be one of the simplest geometric primitives. Using line fitting algorithms, it is possible to identify linear segments in the LiDAR point cloud. This approach is especially useful when linear features are predominant, as happens in indoor environments. Pieces of research such as those conducted by Prieto-Fernández et al. [17], Arras and Siegwart [15], Siadat et al. [20] or Vandorpe et al. [16] contain effective methods for the characterization of straight sections. Line extraction has been used in mapping processes such as those performed by Vandorpe et al. [16], An et al. [32], Pfister et al. [33], or Garulli et al. [34]. Other key points, such as curved sections, have been in the research of Pedraza et al. [35] or Nunez et al. [36], among others. Curve fitting techniques allow algorithms to recognize curvilinear patterns in the point cloud, thus identifying elements such as rounded corners or curved edges.

In this paper, we are particularly concerned with corners. We define a corner as the intersection of line segments. The uncertainty of these geometric features determines overall map quality. This is affected by the accuracy of the data provided by the LiDAR sensor, as well as the effectiveness of the processing algorithms. To tackle the latter, we propose a model for the evaluation of the uncertainty of the representative map points

based on the uncertainty levels provided by the LIDAR sensor. For comparison purposes, we use a classical model, presented in [20].

The methodology proposed in this paper extends the approach presented in [17] by reformulating the line characterization in the inverse complex domain within a Weighted Conformal Total Least Squares framework. In the Weighted Conformal LiDAR-Mapping (WCLM) approach [17], straight lines are represented through the coordinates of a generating point Q in the inverted plane obtained by conformal inversion, and the estimation problem is formulated in terms of these coordinates. A related approach was later proposed in [18], where line fitting is performed using a Conditional Weighted Linear Fitting (CWLF) formulation. In that method, the regression model is conditioned on the accuracy of one coordinate axis, leading to an asymmetric estimation framework. In contrast to classical TLS-based line parameterizations, where the implicit model (a, b, c) is defined up to an arbitrary scale factor, the WCTLS formulation proposed in this work directly estimates the parameters of the implicit line equation while exploiting the geometric relationship with the characteristic point Q. By introducing a geometrically motivated normalization derived from the conformal representation, the scale ambiguity of the implicit model is removed. As a result, the estimation problem can be expressed within a total least squares framework with improved numerical conditioning and more stable covariance propagation, particularly during corner estimation.

3 Methodology

This section describes the methodology adopted for extracting straight-line segments and corner features from 2D LiDAR data, together with their associated covariance matrices. The proposed framework operates on the implicit representation of lines, allowing for a compact geometric description and direct propagation of covariance matrices. Starting from raw LiDAR points, straight segments are first estimated using Total Least Squares-based formulations. These segments are represented in implicit form and subsequently intersected to obtain corner features. The covariance matrix associated with line parameters is propagated to the corner estimates, allowing the reliability of the extracted landmarks to be quantified.

Within this framework, three TLS-based estimation strategies are considered. The first corresponds to the classical formulation by Siadat et al. [20]. The second extends this approach by incorporating range-dependent weighting, as justified in [17]. The third method is the Weighted Conformal Total Least Squares formulation proposed in this work, which introduces a geometric constraint to improve the conditioning of the estimation problem.

For clarity, the overall processing pipeline of the proposed method is summarized in Algorithm 1:

Algorithm 1: WCTLS-based line extraction and corner uncertainty estimation

Require: Set of LiDAR points $\{(\rho_i, \theta_i)\}$
Ensure: Corner coordinates (x_c, y_c) and associated covariance matrices
1: Convert LiDAR measurements from polar to Cartesian coordinates (x_i, y_i)
2: Segment the point cloud into line segments using IEPF segmentation
3: **for** each detected segment **do**
4: Estimate line parameters using WCTLS formulation
5: Compute covariance matrix of line parameters through covariance propagation
6: **end for**
7: **for** each pair of adjacent line segments **do**
8: Compute corner coordinates from line intersection
9: Propagate line covariance matrices to obtain corner covariance matrix

(Continued)

Algorithm 1 (continued)

10: **end for**
11: Compute corner uncertainty measures (standard deviations and ellipse areas)
return Estimated corners and associated uncertainty metrics

3.1 Unweighted Total Least Squares (UTLS)

As a baseline, we adopt the classical Unweighted Total Least Squares formulation for line fitting, as described by Siadat et al. [20]. Given a set of 2D points (x_i, y_i) extracted from the mapped environment, a straight segment is represented using the implicit line equation

$$ax + by + c = 0 \tag{1}$$

where the estimators of the parameters a, b and c are

$$a = \sum_i^n x_i \sum_i^n y_i^2 - \sum_i^n y_i \sum_i^n x_i y_i \tag{2}$$

$$b = \sum_i^n y_i \sum_i^n x_i^2 - \sum_i^n x_i \sum_i^n x_i y_i \tag{3}$$

$$c = \left(\sum_i^n x_i y_i\right)^2 - \sum_i^n x_i^2 \sum_i^n y_i^2 \tag{4}$$

Geometrically, the parameters a, b, and c define the straight line containing the detected segment in implicit form. The pair (a, b) determines the direction of the normal vector to the line, while the parameter c specifies the perpendicular distance of the line from the origin when the normal vector is normalized. Therefore, estimating these parameters corresponds to finding the straight line that best represents the set of LiDAR points belonging to the segment.

Beyond parameter estimation, quantifying the covariance matrix of the fitted line is necessary to assess the reliability of subsequent geometric features, such as corners. Assuming $(\sigma_\rho, \sigma_\theta)$ are the LiDAR measurement standard deviations, the covariance matrix of the line parameters C_U can be obtained through first-order uncertainty propagation

$$C_U = \begin{bmatrix} V_a & C_{ab} & C_{ac} \\ C_{ab} & V_b & C_{bc} \\ C_{ac} & C_{bc} & V_c \end{bmatrix} = J_U \cdot \begin{bmatrix} \sigma_\rho^2 & C_{\rho\theta} \\ C_{\rho\theta} & \sigma_\theta^2 \end{bmatrix} \cdot J_U^T \tag{5}$$

where the Jacobian matrix of line parameters w.r.t. (ρ_i, θ_i) is J_U and the covariance matrix $C_{\rho\theta}$ is null.

$$C_U = \sigma_\rho^2 \cdot \sum_i \begin{bmatrix} R_1^2 & R_1R_2 & R_1R_3 \\ R_2R_1 & R_2^2 & R_2R_3 \\ R_3R_1 & R_3R_2 & R_3^2 \end{bmatrix} + \sigma_\theta^2 \cdot \sum_i \begin{bmatrix} S_1^2 & S_1S_2 & S_1S_3 \\ S_2S_1 & S_2^2 & S_2S_3 \\ S_3S_1 & S_3S_2 & S_3^2 \end{bmatrix} \tag{6}$$

The expressions we have obtained for these terms are

$$R_1 = \frac{N}{\rho_i} \cdot \left(x_i \overline{Y^2} + 2y_i^2 \overline{X} - y_i \overline{XY} - 2x_i y_i \overline{Y}\right) \tag{7a}$$

$$R_2 = \frac{N}{\rho_i} \cdot \left(y_i \overline{X^2} + 2x_i^2 \overline{Y} - x_i \overline{XY} - 2x_i y_i \overline{X} \right) \tag{7b}$$

$$R_3 = \frac{2N}{\rho_i} \cdot \left(2x_i y_i \overline{XY} - x_i^2 \overline{Y^2} - y_i^2 \overline{X^2} \right) \tag{7c}$$

$$S_1 = N \cdot \left(-y_i \overline{Y^2} + 2x_i y_i \overline{X} - x_i \overline{XY} - \left(x_i^2 - y_i^2 \right) \overline{Y} \right) \tag{7d}$$

$$S_2 = N \cdot \left(x_i \overline{X^2} - 2x_i y_i \overline{Y} + y_i \overline{XY} - \left(x_i^2 - y_i^2 \right) \overline{X} \right) \tag{7e}$$

$$S_3 = 2N \cdot \left[\left(x_i^2 - y_i^2 \right) \overline{XY} + x_i y_i \left(\overline{Y^2} - \overline{X^2} \right) \right] \tag{7f}$$

where N is the total number of points.

3.2 Weighted Total Least Squares (WTLS)

The UTLS formulation assumes homoscedastic measurements, which is not consistent with the noise characteristics of 2D LiDAR sensors. In actual measurements, LiDAR uncertainty is range-dependent and anisotropic, with variance increasing as a function of the measured distance. This heteroscedastic behaviour is reflected in a weighted formulation following [17].

Each observation is assigned a weighting factor

$$\omega_i = \frac{1}{(\sigma_\rho \rho_i \sigma_\theta)^2}, \tag{8}$$

which corresponds to the inverse of the measurement variance derived from the probabilistic model of LiDAR measurements in polar coordinates. Assuming independent Gaussian uncertainties in range ρ (measured by the LiDAR sensor) and angle θ (provided by the internal encoder), the resulting measurement distribution can be modeled as a bivariate Gaussian distribution with a diagonal covariance matrix. The weighting factor corresponds to the inverse of the determinant of this covariance matrix, which represents the dispersion of the measurement distribution [17]. This formulation is equivalent to the first-order propagation of polar measurement uncertainty through the polar-to-Cartesian coordinate transformation. This weighting gives lower influence to distant or noisier measurements and improves the statistical consistency of the estimation.

The weighted implicit line model becomes

$$a_w x + b_w y + c_w = 0, \tag{9}$$

where the parameters (a_w, b_w, c_w) are obtained by solving a Weighted Total Least Squares problem

$$a_w = \sum_i^n \omega_i x_i \sum_i^n \omega_i y_i^2 - \sum_i^n \omega_i y_i \sum_i^n \omega_i x_i y_i \tag{10}$$

$$b_w = \sum_i^n \omega_i y_i \sum_i^n \omega_i x_i^2 - \sum_i^n \omega_i x_i \sum_i^n \omega_i x_i y_i \tag{11}$$

$$c_w = \left(\sum_i^n \omega_i x_i y_i \right)^2 - \sum_i^n \omega_i x_i^2 \sum_i^n \omega_i y_i^2 \tag{12}$$

As in the UTLS case, the covariance matrix is propagated to quantify the reliability of the estimated line parameters. The covariance matrix of the weighted parameters C_W is obtained as

$$C_W = \begin{bmatrix} V_{a_w} & C_{a_w b_w} & C_{a_w c_w} \\ C_{a_w b_w} & V_{b_w} & C_{b_w c_w} \\ C_{a_w c_w} & C_{b_w c_w} & V_{c_w} \end{bmatrix} = J_W \cdot \begin{bmatrix} \sigma_\rho^2 & C_{\rho\theta} \\ C_{\rho\theta} & \sigma_\theta^2 \end{bmatrix} \cdot J_W^T \tag{13}$$

where J_W is the Jacobian matrix of line parameters $C(a_w, b_w, c_w)$ w.r.t. (ρ_i, θ_i).

$$C_W = \sigma_\rho^2 \cdot \sum_i \begin{bmatrix} T_1^2 & T_1 T_2 & T_1 T_3 \\ T_2 T_1 & T_2^2 & T_2 T_3 \\ T_3 T_1 & T_3 T_2 & T_3^2 \end{bmatrix} + \sigma_\theta^2 \cdot \sum_i \begin{bmatrix} U_1^2 & U_1 U_2 & U_1 U_3 \\ U_2 U_1 & U_2^2 & U_2 U_3 \\ U_3 U_1 & U_3 U_2 & U_3^2 \end{bmatrix} \tag{14}$$

For these terms, we have obtained the following expressions, where the average values are weighted.

$$T_1 = \frac{\omega_i \sum \omega_i}{\rho_i} \cdot \left(-x_i \overline{Y^2} + y_i \overline{XY}\right) \tag{15a}$$

$$T_2 = \frac{\omega_i \sum \omega_i}{\rho_i} \cdot \left(-y_i \overline{X^2} + x_i \overline{XY}\right) \tag{15b}$$

$$T_3 = 0 \tag{15c}$$

$$U_1 = \omega_i \sum \omega_i \cdot \left(-y_i \overline{Y^2} + 2x_i y_i \overline{X} - x_i \overline{XY} - \left(x_i^2 - y_i^2\right) \overline{Y}\right) \tag{15d}$$

$$U_2 = \omega_i \sum \omega_i \cdot \left(x_i \overline{X^2} - 2x_i y_i \overline{Y} + y_i \overline{XY} - \left(x_i^2 - y_i^2\right) \overline{X}\right) \tag{15e}$$

$$U_3 = 2\omega_i \sum \omega_i \cdot \left[\left(x_i^2 - y_i^2\right) \overline{XY} + x_i y_i \left(\overline{Y^2} - \overline{X^2}\right)\right] \tag{15f}$$

Note that, since $\omega_i \propto 1/\rho_i^2$ and $x_i, y_i \propto \rho_i$, the products $\omega_i x_i^2$, $\omega_i y_i^2$, and $\omega_i x_i y_i$ become independent of ρ_i. Therefore, $\partial c_w / \partial \rho_i = 0$, which explains why $T_3 = 0$ in Eq. (15c).

Compared to UTLS, the weighted formulation better reflects the statistical properties of LiDAR measurements. However, the implicit parameterization still retains a scale ambiguity that can affect the conditioning of the estimation problem, as discussed in the following subsection.

3.3 Weighted Conformal Total Least Squares (WCTLS)

The implicit line parameterization used in UTLS and WTLS exhibits an inherent scale ambiguity, since multiplying (a, b, c) by any non-zero scalar represents the same geometric line. This ambiguity can degrade the numerical conditioning of the estimation and affect uncertainty propagation. To address this limitation, the proposed Weighted Conformal Total Least Squares formulation introduces a geometric normalization derived from the inverse complex representation of the line.

The WCTLS formulation builds upon the inverse complex representation of a line derived from the characteristic point $Q(x_Q, y_Q)$, as introduced in [17]. In this representation, the line passing through the segment can be expressed as

$$-k \cdot x_Q \cdot x + k \cdot y_Q \cdot y + k = 0 \tag{16}$$

where k is an arbitrary scale factor. Instead of leaving this factor undetermined, we impose as a restriction that the orthogonal vector to the straight line containing the segment is unitary. This removes the scale ambiguity and leads to a well-defined geometric parameterization. The normalization factor is therefore chosen as

$$k^2 = \frac{1}{{x_Q}^2 + {y_Q}^2} \tag{17}$$

Considering k as positive, the normalized line equation becomes

$$\check{a}x + \check{b}y + \check{c} = 0 \tag{18}$$

where $\check{a}$ and $\check{b}$ represent the versors (cosine and sine, respectively) of the orthonormal vector, i.e., cosine and sine of the angle that the line segment forms with respect to the OX axis, and $\check{c}$ corresponds to the distance between the straight line containing the segment and the origin of coordinates.

$$\check{a} = \frac{-x_Q}{\sqrt{x_Q^2 + y_Q^2}} \tag{19}$$

$$\check{b} = \frac{y_Q}{\sqrt{x_Q^2 + y_Q^2}} \tag{20}$$

$$\check{c} = \frac{1}{\sqrt{x_Q^2 + y_Q^2}} \tag{21}$$

This parameterization decouples orientation and distance, leading to improved conditioning of the estimation problem and more stable uncertainty propagation.

Following the formulation in WCLM [17], the covariance matrix C_{WC} of the normalized line parameters is obtained from the covariance matrix C_Q of point Q through first-order uncertainty propagation

$$C_{WC} = J_{WC} \cdot C_Q \cdot J_{WC}^T \tag{22}$$

where J_{WC} is defined by

$$J_{WC} = \begin{bmatrix} \frac{\partial \check{a}}{\partial x_Q} & \frac{\partial \check{a}}{\partial y_Q} \\ \frac{\partial \check{b}}{\partial x_Q} & \frac{\partial \check{b}}{\partial y_Q} \\ \frac{\partial \check{c}}{\partial x_Q} & \frac{\partial \check{c}}{\partial y_Q} \end{bmatrix} = \frac{1}{(x_Q^2 + y_Q^2)^{3/2}} \begin{bmatrix} -y_Q^2 & x_Q y_Q \\ -x_Q y_Q & x_Q^2 \\ -x_Q & -y_Q \end{bmatrix} \tag{23}$$

3.4 Corner Estimation

Once straight segments have been estimated, corner features are obtained from the intersection of adjacent lines. Corners constitute salient geometric landmarks in structured environments. The previous three methods define the line containing each segment implicitly from three parameters, obtained by variants of Total Least Squares. The corners of the profile are extracted from these parameters by intersecting adjacent line segments. The procedure followed is the one suggested by [17], using [20] as the basis for straight section characterization.

The corner coordinates (x_c, y_c) are defined as

$$x_c = \frac{b_\xi c_{\xi+1} - b_{\xi+1} c_\xi}{a_\xi b_{\xi+1} - a_{\xi+1} b_\xi} \tag{24}$$

$$y_c = \frac{a_{\xi+1} c_\xi - a_\xi c_{\xi+1}}{a_\xi b_{\xi+1} - a_{\xi+1} b_\xi} \tag{25}$$

where the ξ-th terms correspond to the line parameters containing the first segment, while the $\xi + 1$-th terms refer to the line parameters containing the second segment that forms the corner. Consequently, corner covariance matrices are obtained by propagating the covariance matrices of the parameters corresponding to the involved segments, collected in matrices C_U, C_W and C_{WC} as per the described methodology. The covariance propagation, therefore, quantifies how the uncertainty of the line estimates is transferred to the corner coordinates, providing a measure of the reliability of the detected feature.

4 Results and Discussion

Analysis and comparison of the Total Least Squares methods discussed in the previous section was performed on data captured by SLAMTEC's RPLIDAR S1 sensor. It is a two-dimensional sensor with a range of 40 m and a Field-of-View of 360°. According to the manufacturer, its depth accuracy is 5 cm while its angular resolution is 0.391° [37]. This information has been used in the uncertainty as input for the uncertainty propagation algorithms.

The sensor was operated in a stationary configuration and placed on existing furniture within the environment. In environment A, the sensor was positioned at an approximate height of 1 m above the floor, while in environment B, the height was approximately 1.5 m. In both cases, the sensor remained fixed during the acquisition process. For each environment, 100 consecutive LiDAR scans were acquired from the same position using the standard configuration of the RPLIDAR S1 sensor, operating at a scan frequency of 10 Hz.

The experimental evaluation of the UTLS, WTLS, and WCTLS methods has been conducted in two structured environments, which we have identified as environment A and environment B, as shown in Fig. 1. Environment A, characterized by small dimensions, is approximately 4.5 m long and 2.5 m wide. On the contrary, environment B presents larger dimensions, about 18 m long by 9 m wide. Environment A corresponds to a structured indoor domestic space (room-like scenario) where the dominant geometric elements are walls, columns, and a wardrobe. These elements generate several planar surfaces and orthogonal intersections that produce the line segments and corner features used in the experiments. Environment B corresponds to a laboratory mainly composed of cabinets, columns, and partition panels. This configuration creates multiple parallel walls and partial occlusions typical of indoor workspaces, leading to the set of detectable line segments and corner intersections.

The segmentation of raw data has been performed using the Iterative End Point Fit methodology. A threshold distance of 40 mm has been set for the IEPF algorithm. This value corresponds to an intermediate operating point that yields a sufficient number of geometric features to represent the environment while avoiding over-segmentation of the LiDAR scan. A sensitivity analysis over multiple LiDAR scans showed that increasing the threshold reduces the number of detected corners as expected, while the propagated corner uncertainty and the relative performance of UTLS, WTLS, and WCTLS remain consistent across the tested range.

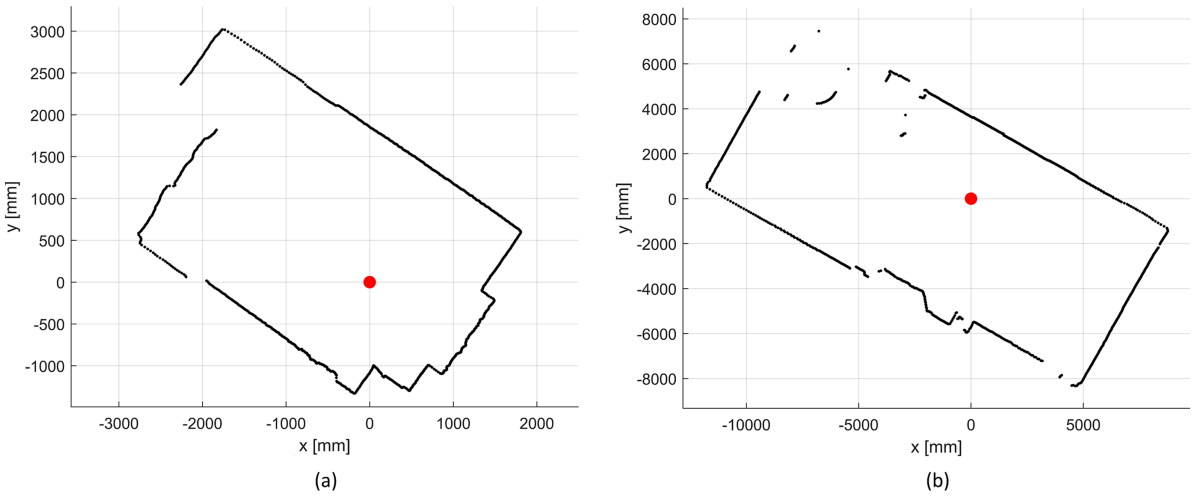

Figure 1: The datasets used in the experiments have been acquired from the RPLiDAR sensor. The mapped profile points are shown in black while the origin of coordinates corresponds to the position of the sensor (red dot) within the mapped environment. (**a**) Environment A. (**b**) Environment B.

To facilitate the geometric interpretation of the results, a representative scan from each environment is first analyzed in detail. This representative-scan analysis is used to illustrate the extracted line segments, corner locations, and associated propagated covariance ellipses. Subsequently, the statistical consistency of the three methods is assessed over the full set of 100 repeated scans acquired in each environment.

The scans yielded by the sensor show a section of both environments in polar coordinates. The origin of coordinates is defined by the sensor position. Environment A is defined by 935 points, which are condensed to 21 segments and 18 corners. Environment B is defined by 36 straight segments and 23 corners, extracted from the 887 points provided by the laser rangefinder. In Fig. 2, both locations are shown with the corners numbered clockwise, since this is the rotational direction of the laser rangefinder.

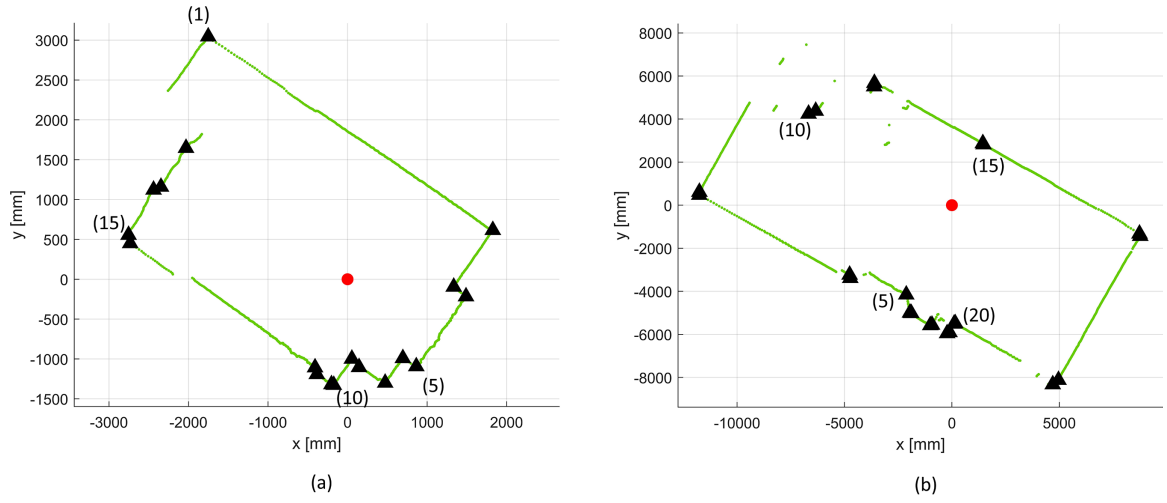

Figure 2: The black triangles represent the corners extracted from the intersection of the environments' straight sections. Environment A has 18 corners while environment B is characterized by 23 corners. (**a**) Environment A. (**b**) Environment B.

Tables 1 and 2 show the standard deviations of the estimated corner coordinates obtained by UTLS, WTLS, and the proposed WCTLS formulation for a representative scan in environments A and B, respectively. For both environments, UTLS and WTLS yield nearly identical standard deviation values for all corners. Differences between both methods remain below a few percent and do not alter the overall magnitude of the uncertainty, confirming that the introduction of measurement weighting alone does not significantly improve the reliability of the extracted corner features.

Table 1: Corner uncertainties of environment A in mm.

Corner	UTLS		WTLS		WCTLS	
	σ_{x_c}	σ_{y_c}	σ_{x_c}	σ_{y_c}	σ_{x_c}	σ_{y_c}
1	42.02	35.08	42.98	37.28	13.43	10.43
2	38.75	46.31	38.38	45.70	8.86	7.18
3	37.45	35.28	37.48	35.27	11.04	12.96
4	38.74	35.15	38.77	35.14	11.76	12.56
5	44.09	29.29	43.97	29.36	13.89	10.21
6	42.52	29.67	42.41	29.71	13.59	11.50
7	40.39	33.50	40.35	33.48	14.14	12.12
8	108.08	102.57	110.27	104.08	41.75	37.57
9	27.27	35.27	27.33	35.31	10.51	13.83
10	37.83	43.36	37.67	43.40	21.46	26.95
11	187.04	97.18	187.14	97.10	84.10	40.56
12	38.77	74.93	39.51	75.36	25.53	32.23
13	42.22	85.81	42.97	85.75	13.33	14.08
14	56.23	51.97	56.20	51.97	33.67	29.03
15	37.57	95.53	37.59	95.84	17.56	40.37
16	78.55	58.15	78.11	57.53	29.05	25.87
17	86.91	62.53	86.53	61.90	35.16	34.73
18	156.12	174.29	156.13	174.26	59.12	66.36

Note: Uncertainties are reported in mm. σ_{x_c} and σ_{y_c} denote the standard deviations of the corner coordinates along the x and y axes, respectively.

Table 2: Corner uncertainties of environment B in mm.

Corner	UTLS		WTLS		WCTLS	
	σ_{x_c}	σ_{y_c}	σ_{x_c}	σ_{y_c}	σ_{x_c}	σ_{y_c}
1	46.59	57.20	46.63	57.21	37.36	51.30
2	88.80	36.59	88.79	36.59	65.74	30.47
3	232.04	124.88	231.13	124.58	127.36	61.92
4	36.28	58.61	36.41	58.66	18.95	42.12
5	40.86	68.15	41.03	68.23	16.55	22.29
6	54.22	67.46	54.26	67.50	43.38	51.52
7	54.52	66.33	54.56	66.35	37.89	41.68
8	49.08	54.08	49.08	53.82	53.34	32.23

(Continued)

Table 2 (continued)

Corner	UTLS		WTLS		WCTLS	
	σ_{x_c}	σ_{y_c}	σ_{x_c}	σ_{y_c}	σ_{x_c}	σ_{y_c}
9	53.57	142.46	53.57	142.51	35.97	69.75
10	171.83	42.70	171.66	42.66	136.69	37.41
11	136.30	89.89	136.22	89.89	87.59	69.42
12	41.29	123.92	41.00	123.30	47.36	100.55
13	34.07	38.74	34.03	38.77	28.50	24.47
14	97.49	100.88	97.28	100.36	45.03	27.95
15	100.19	104.79	100.12	104.35	45.32	28.25
16	62.86	63.33	62.90	63.46	48.09	42.58
17	36.76	89.71	36.76	89.69	33.58	82.10
18	112.84	131.71	112.86	131.72	50.22	82.49
19	90.89	41.36	90.90	41.36	69.83	31.80
20	73.03	36.45	73.15	36.47	47.24	26.80
21	55.88	67.45	55.67	67.33	42.24	46.54
22	56.72	69.15	56.57	69.13	43.90	54.87
23	31.48	43.63	31.48	43.63	32.11	36.14

Note: Uncertainties are reported in mm. σ_{x_c} and σ_{y_c} denote the standard deviations of the corner coordinates along the x and y axes, respectively.

In contrast, the proposed WCTLS formulation reduces the standard deviations of the corner coordinates. In environment A (Table 1), the standard deviations σ_{x_c} and σ_{y_c} obtained with WCTLS are typically reduced by factors ranging from approximately 3 to 6 with respect to UTLS and WTLS. For instance, corner 1 exhibits a reduction from $(42.02, 35.08)$ mm with UTLS to $(13.43, 10.43)$ mm with WCTLS, while corner 18 decreases from $(156.12, 174.29)$ mm to $(59.12, 66.36)$ mm. Similar reductions are observed across the remaining corners, including those associated with comparatively large coordinate standard deviations.

A comparable trend is observed in environment B (Table 2), which presents a more challenging geometric configuration with larger distances and several partial occlusions. While UTLS and WTLS again yield virtually identical results, WCTLS achieves a systematic reduction in the standard deviations of the corner coordinates. Typical reductions range between factors of 2 and 4, depending on the local corner geometry. These results indicate that the improvement introduced by WCTLS is consistent across different indoor environments and not restricted to a particular spatial configuration.

To provide an intuitive visualization of the uncertainty associated with the corner estimates, Fig. 3 shows the covariance ellipses obtained for a scan in both experimental environments. The ellipses represent the propagated covariance of the estimated corner coordinates and are displayed with an expansion factor of 10 to improve visual interpretation. As observed in the figure, the uncertainty ellipses obtained with UTLS and WTLS are nearly identical in most cases, confirming that both formulations lead to similar uncertainty estimates when applied to the considered datasets. A small discrepancy can be observed in corner 1 of Environment A, where the two methods produce slightly different ellipse sizes. However, these differences remain minor compared to the overall uncertainty scale. In contrast, the proposed WCTLS formulation consistently produces smaller uncertainty ellipses for all detected corners in both environments. This reduction indicates that the proposed normalization strategy improves the conditioning of the estimation

problem and leads to more stable covariance propagation in the corner estimation process. Consequently, although all methods provide equivalent geometric corner locations, WCTLS achieves a consistent reduction in the estimated positional uncertainty of the extracted features. This visual result is fully consistent with the numerical values reported in Tables 1 and 2.

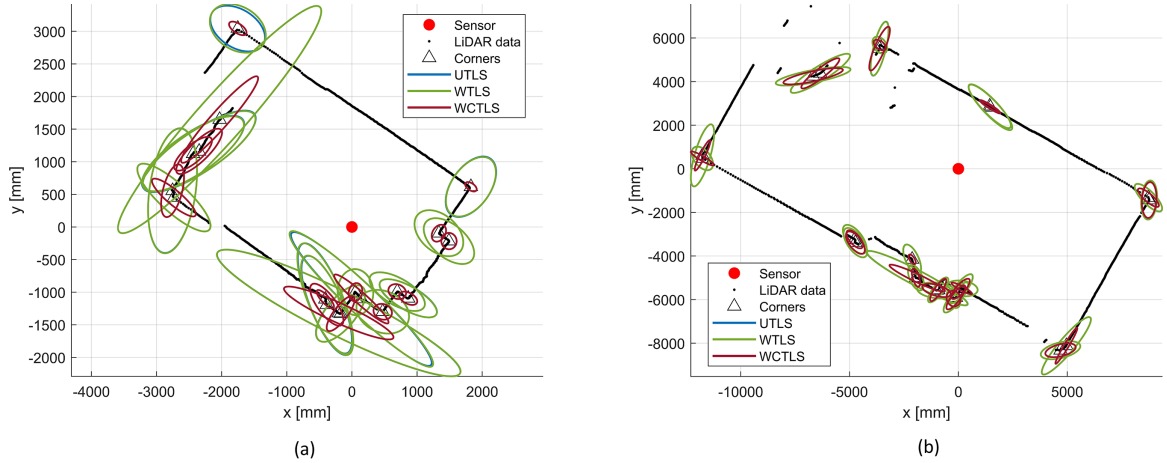

Figure 3: Corner uncertainty ellipses obtained from a LiDAR scan in the two experimental environments: (**a**) Environment A and (**b**) Environment B. Ellipses correspond to UTLS (blue), WTLS (green), and WCTLS (red) and are shown with a scaling factor of 10 for visualization.

Although the representative-scan analysis is useful to visualize the geometric behavior of the three methods, it does not by itself characterize scan-to-scan variability. For this reason, an additional repeatability analysis was conducted using 100 consecutive scans acquired from a fixed sensor position in each environment. For each scan, the median area of the uncertainty ellipses corresponding to the detected corners was computed. This per-scan median ellipse area provides a compact scalar measure of the typical propagated corner uncertainty while ensuring that each scan contributes equally to the statistical analysis, independently of the number of corners detected in that scan. Fig. 4 shows the statistical distribution of these per-scan median ellipse areas for the three estimation methods. Each box represents the interquartile range, corresponding to the interval between the first and third quartiles and therefore containing the central 50% of the scans. The horizontal line inside each box denotes the median value, while the whiskers extend to 1.5 times the interquartile range. Outliers, corresponding to scans with unusually large uncertainty values, are represented by circles. A logarithmic scale is used in the vertical axis to facilitate the visualization of relative differences in uncertainty magnitude.

In environment A, the box plots in Fig. 4a show that UTLS and WTLS yield very similar uncertainty levels across the repeated scans. The median ellipse area per scan is approximately $4.5 \times 10^3\,\mathrm{mm}^2$ for both methods, with values of $4498.5 \pm 330.3\,\mathrm{mm}^2$ and $4594.7 \pm 355.0\,\mathrm{mm}^2$, respectively. In contrast, the proposed WCTLS formulation produces a substantial reduction in the typical uncertainty, yielding a median ellipse area per scan of $626.2 \pm 178.7\,\mathrm{mm}^2$. This corresponds to an approximate sevenfold reduction in the typical per-scan median ellipse area with respect to the classical TLS formulations. The box plot also reveals a noticeably smaller dispersion of the uncertainty values for WCTLS, indicating a more stable behavior across repeated scans.

A similar trend is observed in environment B, as shown in Fig. 4b. In this case, UTLS and WTLS again exhibit nearly identical behavior, with median ellipse areas per scan of $8125.3 \pm 914.1\,\mathrm{mm}^2$ and $8123.6 \pm 911.1\,\mathrm{mm}^2$, respectively. The WCTLS method consistently produces lower uncertainty values, with

a median ellipse area per scan of $3468.5 \pm 640.9\,\mathrm{mm}^2$. Although the improvement is less pronounced than in environment A, WCTLS still reduces the typical uncertainty by a factor of approximately 2.3. The box plot distributions further show that this reduction is systematic across the repeated scans, rather than being driven by a small number of favorable cases.

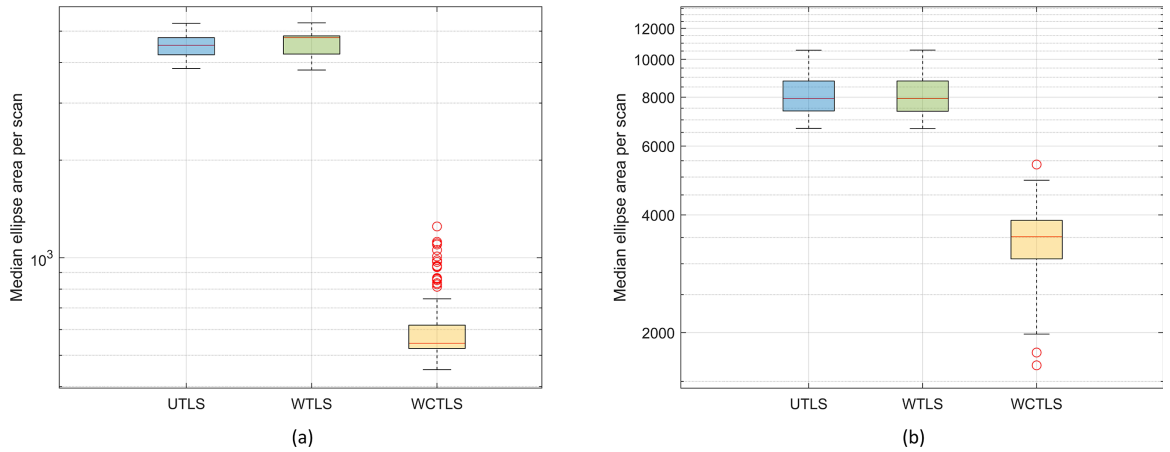

Figure 4: Distribution of the median corner uncertainty ellipse area per scan obtained from 100 repeated scans in two indoor environments: (**a**) Environment A and (**b**) Environment B. Each value corresponds to one scan and represents the median ellipse area of the corners detected in that scan. The vertical axis is displayed in logarithmic scale.

The experimental results show that this improvement in WCTLS does not come from the weighting of measurements, which is already present in WTLS, but from the elimination of the scale ambiguity inherent in the implicit line representation used in classical TLS formulations. In UTLS and WTLS, the parameters (a, b, c) are not uniquely defined, which negatively affects numerical conditioning and amplifies the propagated covariance associated with the corner estimates. By enforcing a geometrical normalization, the WCTLS formulation decouples orientation and distance parameters and yields better-conditioned covariance matrices. This results in smaller and less anisotropic error ellipses, as evidenced both by the per-corner uncertainty values and by the global ellipse area distributions.

5 Conclusions

Simplifying the 2D LiDAR SLAM process by extracting geometric primitives from the mapped environment is becoming increasingly common. In this paper we have analyzed different variants of the Total Least Squares method for obtaining geometric features in the mapping process, proposing a method that improves the conditioning of the estimation problem and the reliability of the extracted geometric features.

Experimental results obtained from two real indoor environments show that all analyzed TLS variants (UTLS, WTLS, and WCTLS) yield equivalent geometric positions for the extracted corners. This confirms that the proposed method does not alter the underlying geometric structure of the map. However, significant differences arise in the associated covariance-based uncertainty estimates. While UTLS and WTLS provide nearly identical uncertainty values, the proposed WCTLS formulation consistently achieves a reduction in the standard deviations of the estimated corner coordinates. The standard deviations of the corner coordinates obtained with WCTLS are reduced by factors ranging from approximately 3 to 6 in environment A and between 2 and 4 in environment B when compared to UTLS and WTLS. This improvement is further supported by the analysis of the propagated error ellipse areas computed over 100 repeated scans acquired from fixed sensor positions. In this repeatability analysis, WCTLS significantly reduces the typical

ellipse area and exhibits lower dispersion across scans, indicating a more stable behavior of the propagated uncertainty estimates.

These results demonstrate that the improvement achieved by WCTLS is not driven by measurement weighting alone, but by the elimination of the scale ambiguity inherent to the implicit line representation used in conventional TLS approaches. By enforcing a geometric normalization, WCTLS yields better-conditioned covariance matrices and more compact uncertainty estimates for derived corner features.

Despite these promising results, the proposed formulation has been validated in structured indoor environments, where geometric primitives such as lines and corners are clearly observable. Further investigation will be necessary to assess whether the approach can be generalized to more complex or less structured scenarios. It should be noted that no external ground-truth measurements of the true corner positions were available in the considered environments. Consequently, the experimental results demonstrate a consistent reduction in the propagated uncertainty associated with the extracted corners, but they do not directly establish an improvement in absolute geometric accuracy with respect to an external reference.

Future work will focus on exploiting the improved corner uncertainty provided by WCTLS in downstream SLAM tasks, such as data association, map optimization, and robot localization, assessing its potential impact on overall navigation accuracy and robustness.

Acknowledgement: The authors would like to express their sincere gratitude to the University of León for its institutional support and to TRESCA Ingeniería S.A. for its collaboration and support in the development of this research.

Funding Statement: This research was supported by TRESCA Ingeniería S.A. within the framework of the Research Project on *Survey Systems for Hostile Structured Environments Using Simultaneous Localization and Mapping (SLAM) Systems with Lidar Technology*. The project was co-financed by the ERDF, Thematic Objective 1, which seeks to promote technological development, innovation and quality research, and in part by the Regional Government of Castilla y León, through the institute for the Business Competitiveness of Castilla y León (ICE).

Author Contributions: Conceptualization, Natalia Prieto-Fernández and Martín Bayón-Gutiérrez; methodology, Natalia Prieto-Fernández, Sergio Fernández-Blanco and Álvaro Fernández-Blanco; software, Martín Bayón-Gutiérrez; validation, José Alberto Benítez-Andrades; formal analysis, Natalia Prieto-Fernández, Sergio Fernández-Blanco and Álvaro Fernández-Blanco; investigation, Natalia Prieto-Fernández; resources, Francisco Carro-De-Lorenzo; data curation, Natalia Prieto-Fernández; writing—original draft preparation, Natalia Prieto-Fernández, Álvaro Fernández-Blanco and Martín Bayón-Gutiérrez; writing—review and editing, Sergio Fernández-Blanco, Francisco Carro-De-Lorenzo and José Alberto Benítez-Andrades; visualization, Martín Bayón-Gutiérrez; supervision, Francisco Carro-De-Lorenzo and José Alberto Benítez-Andrades; project administration, Natalia Prieto-Fernández; funding acquisition, Natalia Prieto-Fernández. All authors reviewed and approved the final version of the manuscript.

Availability of Data and Materials: Data available on request from the authors.

Ethics Approval: Not applicable.

Conflicts of Interest: The authors declare no conflicts of interest.

References

1. Cheng J, Zhang L, Chen Q, Hu X, Cai J. A review of visual SLAM methods for autonomous driving vehicles. Eng Appl Artif Intell. 2022;114(5):104992. doi:10.1016/j.engappai.2022.104992.
2. Singandhupe A, La HM. A review of slam techniques and security in autonomous driving. In: 2019 Third IEEE International Conference on Robotic Computing (IRC). Piscataway, NJ, USA: IEEE; 2019. p. 602–7.

3. Bastos D, Monteiro PP, Oliveira AS, Drummond MV. An overview of LiDAR requirements and techniques for autonomous driving. In: 2021 Telecoms Conference (ConfTELE). Piscataway, NJ, USA: IEEE; 2021. p. 1–6.
4. Zhou X, Huang R. A state-of-the-art review on SLAM. In: International Conference on Intelligent Robotics and Applications. Cham, Switzerland: Springer; 2022. p. 240–51.
5. Ebadi K, Bernreiter L, Biggie H, Catt G, Chang Y, Chatterjee A, et al. Present and future of SLAM in extreme environments: the DARPA subT challenge. IEEE Trans Robot. 2023;40(2):936–59. doi:10.1109/tro.2023.3323938.
6. Belkin I, Abramenko A, Yudin D. Real-time lidar-based localization of mobile ground robot. Procedia Comput Sci. 2021;186:440–8. doi:10.1016/j.procs.2021.04.164.
7. Francis S, Anavatti SG, Garratt M, Abbass HA. Real-time multi-obstacle detection and tracking using a vision sensor for autonomous vehicle. In: Communication and Intelligent Systems: Proceedings of ICCIS 2020. Cham, Switzerland: Springer; 2021. p. 873–83.
8. Koval A, Kanellakis C, Nikolakopoulos G. Evaluation of Lidar-based 3D SLAM algorithms in SubT environment. IFAC-PapersOnLine. 2022;55(38):126–31. doi:10.1016/j.ifacol.2023.01.144.
9. Khan MU, Zaidi SAA, Ishtiaq A, Bukhari SUR, Samer S, Farman A. A comparative survey of LiDAR-SLAM and lidar based sensor technologies. In: 2021 Mohammad Ali Jinnah University International Conference on Computing (MAJICC). Piscataway, NJ, USA: IEEE; 2021. p. 1–8.
10. Zou Q, Sun Q, Chen L, Nie B, Li Q. A comparative analysis of LiDAR SLAM-based indoor navigation for autonomous vehicles. IEEE Trans Intell Transport Syst. 2021;23(7):6907–21. doi:10.1109/tits.2021.3063477.
11. Kim G, Yun S, Kim J, Kim A. SC-LiDAR-SLAM: a front-end agnostic versatile lidar slam system. In: 2022 International Conference on Electronics, Information, and Communication (ICEIC). Piscataway, NJ, USA: IEEE; 2022. p. 1–6.
12. Li Y, Olson EB. Extracting general-purpose features from LIDAR data. In: 2010 IEEE International Conference on Robotics and Automation. Piscataway, NJ, USA: IEEE; 2010. p. 1388–93.
13. Ali W, Liu P, Ying R, Gong Z. A feature based laser SLAM using rasterized images of 3D point cloud. IEEE Sens J. 2021;21(21):24422–30. doi:10.1109/jsen.2021.3113304.
14. Núñez P, Vázquez-Martín R, Del Toro J, Bandera A, Sandoval F. Natural landmark extraction for mobile robot navigation based on an adaptive curvature estimation. Robot Autonom Syst. 2008;56(3):247–64. doi:10.1016/j.robot.2007.07.005.
15. Arras KO, Siegwart RY. Feature extraction and scene interpretation for map-based navigation and map building. In: Mobile robots XII. Vol. 3210. Bellingham, WA, USA: SPIE; 1998. p. 42–53.
16. Vandorpe J, Van Brussel H, Xu H. Exact dynamic map building for a mobile robot using geometrical primitives produced by a 2D range finder. In: Proceedings of IEEE International Conference on Robotics and Automation.. Piscataway, NJ, USA: IEEE; 1996. Vol. 1, p. 901–8.
17. Prieto-Fernández N, Fernández-Blanco S, Fernández-Blanco Á, Benítez-Andrades JA, Carro-De-Lorenzo F, Benavides C. Weighted conformal LiDAR-mapping for structured SLAM. IEEE Trans Instrument Measur. 2023;72:1–10. doi:10.1109/tim.2023.3284143.
18. Prieto-Fernández N, Fernández-Blanco S, Fernández-Blanco Á, Benítez-Andrades JA, Carro-De-Lorenzo F, Benavides C. Conditional weighted linear fitting for 2D-LiDAR-mapping of indoor SLAM. IEEE Trans Indust Inform. 2024;20(7):9579–87.
19. Yan RJ, Wu J, Yuan Q, Yuan C, Luo LP, Shin KS, et al. Natural corners-based SLAM with partial compatibility algorithm. Proc Instit Mech Eng Part I J Syst Control Eng. 2014;228(8):591–611. doi:10.1177/0959651814533533.
20. Siadat A, Kaske A, Klausmann S, Dufaut M, Husson R. An optimized segmentation method for a 2D laser-scanner applied to mobile robot navigation. IFAC Proc Vol. 1997;30(7):149–54. doi:10.1016/s1474-6670(17)43255-1.
21. Nguyen V, Gächter S, Martinelli A, Tomatis N, Siegwart R. A comparison of line extraction algorithms using 2D range data for indoor mobile robotics. Autonom Rob. 2007;23:97–111.
22. Pavlidis T, Horowitz SL. Segmentation of plane curves. IEEE Trans Comput. 1974;100(8):860–70.
23. Duan D, Xie M, Mo Q, Han Z, Wan Y. An improved Hough transform for line detection. In: 2010 International Conference on Computer Application and System Modeling (ICCASM 2010). Piscataway, NJ, USA: IEEE; 2010. Vol. 2, p. V2-354–7.

24. Fischler MA, Bolles RC. Random sample consensus: a paradigm for model fitting with applications to image analysis and automated cartography. Communicat ACM. 1981;24(6):381–95. doi:10.1145/358669.358692.
25. Liu Y, Emery R, Chakrabarti D, Burgard W, Thrun S. Using EM to learn 3D models of indoor environments with mobile robots. In: The Eighteenth International Conference on Machine Learning. Burlington, MA, USA: Morgan Kaufmann; 2001. p. 329–36.
26. Duda RO, Hart PE. Pattern classification and scene analysis. Vol. 3. New York, NY, USA: Wiley; 1973.
27. Borges GA, Aldon MJ. Line extraction in 2D range images for mobile robotics. J Intell Robot Syst. 2004;40(3):267–97. doi:10.1023/b:jint.0000038945.55712.65.
28. Peter M, Jafri S, Vosselman G. Line segmentation of 2D laser scanner point clouds for indoor slam based on a range of residuals. ISPRS Ann Photogramm Remote Sens Spat Inform Sci. 2017;4:363–9.
29. Li Z, Zuo R, Wang Y, Ding F, Wei C, Wu M. Odometry-assisted LiDAR-openstreetmap matching method for vehicle global positioning. IEEE Internet Things J. 2026;13(8):16303–17. doi:10.1109/jiot.2026.3659142.
30. Deng B, He Y, Shen Z, Zhang Y, Deng Q, Nie Z, et al. YCNNet: road target recognition method by fusion of LiDAR and thermal infrared camera. IEEE Sen J. 2025;26(2):3278–88.
31. Park SH, Yi SY. Least-square matching for mobile robot SLAM based on line-segment model. Int J Cont Autom Syst. 2019;17:2961–8.
32. An SY, Kang JG, Lee LK, Oh SY. SLAM with salient line feature extraction in indoor environments. In: 2010 11th International Conference on Control Automation Robotics & Vision. Piscataway, NJ, USA: IEEE; 2010. p. 410–6.
33. Pfister ST, Roumeliotis SI, Burdick JW. Weighted line fitting algorithms for mobile robot map building and efficient data representation. In: 2003 IEEE International Conference on Robotics and Automation (Cat. No. 03CH37422). Piscataway, NJ, USA: IEEE; 2003. Vol. 1, p. 1304–11.
34. Garulli A, Giannitrapani A, Rossi A, Vicino A. Mobile robot SLAM for line-based environment representation. In: Proceedings of the 44th IEEE Conference on Decision and Control. Piscataway, NJ, USA: IEEE; 2005. p. 2041–6.
35. Pedraza L, Rodriguez-Losada D, Matia F, Dissanayake G, Miró JV. Extending the limits of feature-based SLAM with B-splines. IEEE Trans Robot. 2009;25(2):353–66. doi:10.1109/tro.2009.2013496.
36. Nunez P, Vazquez-Martin R, Bandera A, Sandoval F. An algorithm for fitting 2-D data on the circle: applications to mobile robotics. IEEE Signal Process Lett. 2008;15:127–30. doi:10.1109/lsp.2007.912964.
37. Slamtec. RPLIDAR S1 Datasheet. 2021 [cited 2026 Mar 20]. Available from: http://bucket.download.slamtec.com/f19ea8efcc2bb55dbfd5839f1d307e34aa4a6ca0/LD601_SLAMTEC_rplidar_datasheet_S1_v1.4_en.pdf.